applied sciences

MDPI

Article

Experimental Investigation on the Anchorage Performance of a Tension–Compression-Dispersed Composite Anti-Floating Anchor

Yuguo Liu [1], Kai Xia [2], Botong Wang [2], Ji Le [1], Yanqing Ma [1] and Mingli Zhang [2,*]

[1] China Construction Fourth Engineering Bureau Co., Ltd., Guangzhou 510000, China; sjlyg@cscec.com (Y.L.); xiemengshu1992@outlook.com (J.L.); 15730352696@163.com (Y.M.)
[2] Key Laboratory of Disaster Prevention and Mitigation in Civil Engineering of Gansu Province, Lanzhou University of Technology, Lanzhou 730050, China; 17361565823@163.com (K.X.); botong0233@163.com (B.W.)
* Correspondence: mlzhang@lut.edu.cn

Abstract: Rapid advancements in construction technologies have accelerated the development of complex and deep underground structures, raising concerns about the impact of groundwater on structures, particularly anti-floating measures. Traditional tensioned anchors, commonly used for preventing flotation, suffer from limitations like low pull-out bearing capacity, shallow critical anchoring depth, and localized stress concentration. To overcome these limitations, this paper introduces a tension–compression dispersed composite anchor, which combines casing, load-bearing plates, and tensioned anchors. Comparative tests were conducted between these composite anchors and traditional tensioned anchors to analyze their anchoring behavior. Our results show that tensioned anchors exhibit a stable axial force distribution as anchoring length increases. By identifying abrupt changes in the axial force curve, optimal anchoring lengths for load-dispersed anchors can be determined, thereby enhancing rock and soil strength utilization. The tension–compression-dispersed composite anchor outperforms tensioned anchors, with 1.44 times the ultimate bearing capacity for equivalent anchoring lengths and 1.1 times the capacity for an additional 1 m length. It also displays superior deformation adaptability and structural ductility under high-bearing loads compared to tensioned anchors with extended anchoring lengths. Effectively mobilizing the strength of the lower anchoring segment within the rock and soil results in a lower critical anchoring depth and a more uniform distribution of lateral friction resistance. In conclusion, the tension–compression-dispersed composite anchor offers significant advantages, making it a promising engineering solution for anti-floating anchor systems in complex underground environments.

Keywords: foundation pit engineering; anchoring performance; field test; ultimate bearing capacity; distribution law of axial force

check for updates

Citation: Liu, Y.; Xia, K.; Wang, B.; Le, J.; Ma, Y.; Zhang, M. Experimental Investigation on the Anchorage Performance of a Tension–Compression-Dispersed Composite Anti-Floating Anchor. *Appl. Sci.* **2023**, *13*, 12016. https://doi.org/10.3390/app132112016

Academic Editors: Qian Fang and Pengfei Li

Received: 23 September 2023
Revised: 25 October 2023
Accepted: 2 November 2023
Published: 3 November 2023

Copyright: © 2023 by the authors. Licensee MDPI, Basel, Switzerland. This article is an open access article distributed under the terms and conditions of the Creative Commons Attribution (CC BY) license (https://creativecommons.org/licenses/by/4.0/).

1. Introduction

The continuous growth and utilization of underground spaces have led to the emergence of the concept of the "underground city", which encompasses a wide range of diverse and large-scale underground structures [1–3]. Consequently, the number and duration of human activities in underground spaces have also multiplied, while standards of and demand for these spaces have increased. Furthermore, with the ongoing development of deep, large-scale, and complex underground environments, the issue of groundwater buoyancy affecting the stability of foundation pit excavations and underground buildings and structures has become increasingly significant, making the stability of foundation pit excavation and structural anchorage a crucial aspect of underground engineering construction [4–6]. Geotechnical anchoring has gained widespread application in foundation pits, tunnels, roadways, and other underground engineering projects due to its capability to enhance the stability of rock–soil masses by utilizing their strength and effectively reinforcing their structures.

Anti-floating anchors, as a type of geotechnical anchorage, find extensive application in foundation pit anti-flotation projects due to their advantages of simple construction and cost-effectiveness, and their ability to effectively harness the strength of the geotechnical body, reinforcing both the geotechnical body itself and building structures [7,8]. To enhance the adaptability and cost-effectiveness of anchors under various working conditions, several advancements have been proposed, including pressure prestressing anchors, grouting and mechanical prestressing anchors, rebar splicing couplers, resin rolls, fast-hardening cement roll anchors, hollow grouting anchors, and friction anchors [9]. As a result, the variety of anchors has increased, and the processes have improved. Yang et al. [10] and Huang et al. [11] conducted indoor model tests and on-site prototype tests on an independently developed plate-supported anchor rod. Their research demonstrates that plate-supported anchor rods effectively mobilize endplate resistance, thereby enhancing the anchor rod's ultimate load-bearing capacity. Zhang et al. [12], Sun et al. [13], and Bai et al. [14] conducted comprehensive research on glass fiber-reinforced polymer (GFRP) anchor rods, thoroughly investigating the load transfer mechanisms and pullout resistance of GFRP anchor rods. Their findings indicate the favorable durability and cost-effectiveness of GFRP anchor rods, rendering them suitable for a wide range of applications in engineering projects, such as slope reinforcement and excavation support. However, the above-mentioned anchors have not achieved load distribution, and the strength of the rock mass below the anchor body has not been fully utilized.

Traditional tension or compression anchors suffer from stress concentration at the loaded end due to the decreasing axial force caused by the load acting on the anchor or tie itself. This means that as the load is applied to the anchor, the section of soil or rock at the far end, which is anchored, may not have fully utilized its strength, while the near end, which is also anchored, may have already experienced failure. Consequently, the strength of the soil or rock cannot be fully mobilized [15–17]. The load-spreading anchor effectively distributes the load across individual anchoring segments, thus preventing local stress concentration and enhancing anchoring performance [18]. Jia et al. [19] He et al. [20] conducted experimental analysis and theoretical research on the anchoring mechanism and engineering application of load-dispersing anchors with a single force form. The results demonstrated the high anchoring efficiency of load-dispersed anchors with a single stress form, facilitating stress and deformation coordination within underground structures and reducing project costs. As a permanent structure, it offers evident technical advantages. Wu et al. [21] investigated the anchoring mechanism and engineering application of tension–compression-dispersed anchor cables, establishing stable and reliable load transfer in engineering applications with positive outcomes. Chen et al. [22] conducted a comparative test between tension–compression-dispersed anchor cables and tension anchor cables, revealing a significantly higher ultimate bearing capacity for tension–compression-dispersed anchor cables, enabling better control of anchor cable displacement and improved adaptability for projects with higher anchorage deformation requirements. Tu et al. [23] conducted theoretical and experimental research on the anchorage performance of tension–compression composite anchors, demonstrating that the ultimate bearing capacity of composite anchors exceeds twice that of tension anchors, effectively mitigating local stress concentration and exhibiting good deformation resistance. There are still few studies on load-distributing composite anchors, and the load-bearing performance of this new anchor needs to be further explored.

The aforementioned studies on load-dispersed anchors have demonstrated their favorable anchoring performance. However, existing research predominantly focuses on load-dispersed anchors with a single stress form. There are a limited number of experimental and theoretical investigations concerning tension–compression composite anchors with a simple structure, which can effectively mitigate local stress concentration and enhance ultimate bearing capacity. Therefore, this paper presents an innovative approach in the field of geotechnical engineering. The innovative tension–compression decentralized composite anchor introduced in this study overcomes the constraints of current anchor designs and

provides a practical solution for deep foundation pit projects with shallow groundwater levels. Extensive field testing and comparative analysis with traditional tension anchors demonstrate a substantial improvement in anchoring performance, emphasizing the potential for a new era in anchor systems. This research provides valuable insights for practical applications. Additionally, it provides robust groundwork for further exploration and development in the field of geotechnical engineering. The contributions of this study have the potential to reshape how we approach anchoring in complex and challenging environments, providing new possibilities and enhanced stability for future construction projects.

2. Materials and Methods

2.1. Test Site

The test site is located at the construction site of a deep foundation pit in a sewage treatment plant in Lanzhou, with a total planned land area of 108,211.0 m^2. The construction scale of the project in the near term, by 2025, is a processing capacity of 300,000 $m^3 \cdot d^{-1}$, and in the long term, by 2035, a processing capacity of 400,000 $m^3 \cdot d^{-1}$. The intended project involves an integral buried steel–concrete box structure with a burial depth of approximately 18 to 20 m. The base gradually rises from south to north, with the site's leveled elevation ranging from 1526.50 m to 1529.00 m. The project's importance level is classified as Level I. The site is situated in the high floodplain zone on the left bank of the Yellow River, with a relatively shallow groundwater depth, which affects the project to a certain extent. The surrounding area is characterized by the presence of municipal roads, municipal pipelines, and buildings, contributing to moderately complex environmental conditions. Frequent human engineering activities have led to general environmental degradation, resulting in a Level II complexity rating for the site. The geological composition of the site includes various types of rock and soil, along with relatively thick layers of artificial fill that are unevenly distributed. This non-uniform distribution has led to significant variations in the properties of slope materials. As a result, the complexity level of the foundation is categorized as Level II. The soil layers at the site, from top to bottom, consist of miscellaneous fill, loess-like silt, cobbles, heavily weathered mudstone, and moderately weathered mudstone, as depicted in Figure 1. The stable groundwater depth at the site ranges from approximately 4.8 to 8.3 m, with corresponding elevations between 1519.27 and 1521.24 m. The elevation of the bottom plate of the underground structure ranges from 1507.70 to 1512.30 m, positioned within the influence range of the groundwater up to a certain height. Consequently, anti-floating anchors need to be employed to mitigate buoyancy effects.

The test anchor is positioned within the medium-weathered mudstone layer, specifically at the base of the buried concrete box. The medium-weathered mudstone is characterized by a muddy composition with a thick laminated structure. It exhibits relative integrity but is prone to fracturing and softening, especially when exposed to water. The physical and mechanical parameters of the medium-weathered mudstone are presented in Table 1.

Table 1. Physical mechanical parameters of rock.

Gravity ($kN \cdot m^{-3}$)	The Angle of Internal Friction (°)	Force of Cohesion (kPa)	Elastic Modulus (GPa)	Poisson Ratio	Saturated Compressive Strength (MPa)
21.3	34.7	80	1.7	0.18	0.88

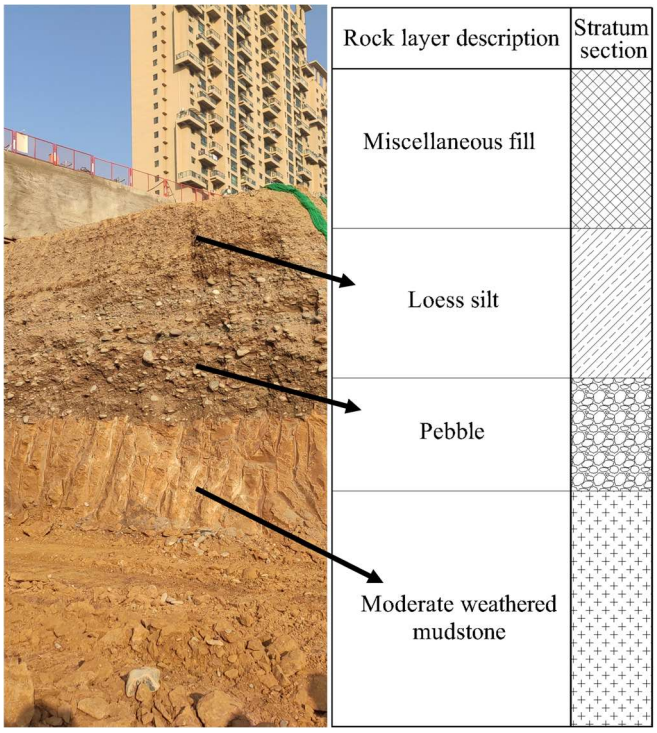


Figure 1. A photo of the conditions of the in situ test.

2.2. Tensile–Compressive Dispersed Composite Anchors

Conventional load-concentrated anchors exhibit a gradual decrease in axial force along the load section towards the far end (for tension anchors, force is transmitted from the beginning to the end of the anchorage section, whereas for pressure anchors, it is transmitted from the end to the beginning), resulting in pronounced stress concentration at the load transfer initiation point [24–26]. When the shear stress surpasses the ultimate bond strength of the interface, the interface tends to soften [27–29] or experience progressive failure [30] Moreover, due to the attenuation of shear stress along the anchorage length, the bond strength of the rear interface in the anchorage section remains underutilized, leading to a low pull-out bearing capacity of the anchor, which poses significant challenges in large-scale engineering applications [31–33]. To optimize the force transmission mechanism of load-concentrated anchors, a single-hole composite anchor has been developed. This innovative anchor design involves dividing the anchorage section of the load-concentrated anchor into multiple unit anchorage sections, each featuring an independent anchor body, free length, and effective anchorage length. The load is simultaneously applied to the anchoring sections of each unit, ensuring uniform stress distribution and load-bearing capacity across all units. This approach effectively addresses issues associated with local stress concentration, shallow critical anchorage depth, and low ultimate bearing capacity observed in load-concentrated anchors.

Considering the factors mentioned above, this study introduces a tension–compression decentralized composite anchor (referred to as the composite anchor hereafter), as illustrated in Figure 2. The anchor is composed of several components including an anchor body, steel casing, bearing plate, and grouting body. The steel casing and bearing plate are welded at the midpoint of the anchor body. The anchorage section comprises three individual sections: tension Section 1 #, the compression section, and tension Section 2 #. In the tension section, the anchor body is bonded to the grouting body, with the axial force gradually decreasing along the anchorage section. The steel casing is positioned on the outer side of the anchor body in the pressure-bearing section, preventing bonding between the anchor body and the grouting body. This configuration facilitates further transmission of the anchor head load to the lower anchorage section, fully utilizing the strength of the rock

and soil mass in the lower part of the anchorage section, thereby addressing the drawback of shallow critical anchorage depth. The bearing plate divides the load transmitted to it into two parts: upward to the pressure section, and downward to tension Section 2 #, effectively reducing local stress concentration. Under the action of the bearing plate, the bearing section undergoes radial deformation upon loading, increasing the normal stress and enhancing the side friction resistance of the anchor. Additionally, the grouting body is less prone to cracking under pressure, preventing groundwater infiltration and corrosion, thus extending the service life of the anchor. To ensure adequate load-bearing capacity, the bearing plate has a thickness of 5 cm. Strengthening the weld between the steel bar and the bearing plate to withstand upper loads involves processing welding holes that connect to two round plates—one with a smaller diameter at the center and larger diameters on both sides. This arrangement ensures sufficient welding strength. To ensure the smooth passage of the steel bar through the steel casing without contact, the steel pipe has a diameter 2 cm greater than that of the steel bar. Consequently, the length of each unit's anchoring section is reduced, effectively mitigating bonding weakening effects and maximizing the utilization of the rock and soil strength within the anchorage section.

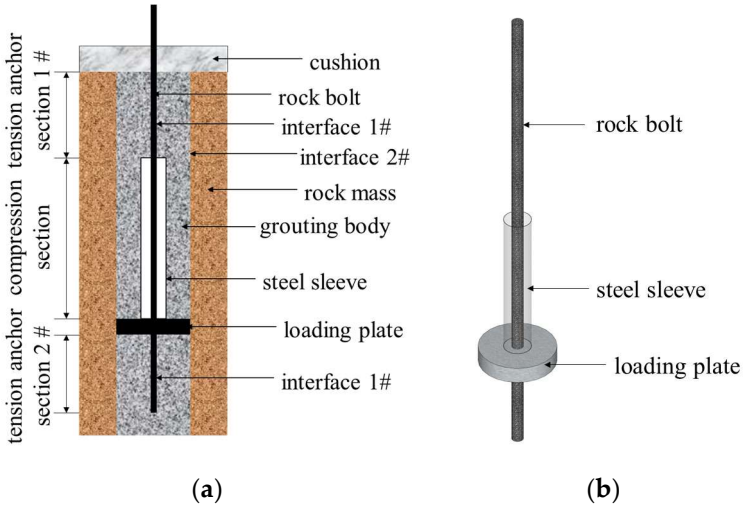


Figure 2. The structure of the tension–compression-dispersed composite anchor: (**a**) schematic representation of the rock and anchor structure; (**b**) composite anchor structure. Where symbol # represents the number of the tension anchoring section.

2.3. Experimental Design

The anchoring mechanism of tension–compression composite anchors displays notable distinctions when contrasted with that of traditional anchors. Currently, there is limited existing research in this field, and there is an urgent requirement for thorough investigation. To gain a comprehensive understanding of the load-carrying characteristics of the new tension–compression-dispersed composite anchors and their distinctions from traditional tension-only and compression-only anchors, full-scale field tests were performed. Traditional tension anchors were employed as a control group, and a thorough analysis and examination were conducted on the anchoring performance of the tension–compression-dispersed composite anchors. To enable a comprehensive comparison, the experiment involved the design of four anchor groups. The first group consisted of composite anchors, while the second to fourth groups were tension anchors. The composite anchor had an effective anchorage length of 3 m, with each tension section measuring 0.75 m in length and the compressive section spanning 1.5 m. To create a non-adhesive section (compressive section), a bearing plate and a 1.5 m long steel casing were welded at the 2.25 m mark on the anchor body. The bearing plate, with a thickness of 5 cm and a diameter of 19 cm (smaller than the anchor hole diameter to ensure smooth insertion), had a hole shape formed by two round tables meeting on the top surface to ensure strong welding seams.

The steel casing used was a 6 cm diameter steel pipe with a wall thickness of 2.5 mm. In the experimental procedure, the drilling sites, hole diameters, and depths were determined based on the geological conditions obtained from survey data. After drilling the anchor holes, the anchors were positioned in the holes according to pre-established locations with the assistance of a crane. Following this, grouting was performed using a cement grout mixture. Ordinary Portland cement was used, and a rust inhibitor for steel reinforcement was included. The grouting process was conducted iteratively, with the addition of fresh grout when the preceding grout had settled, until the entire anchor hole was entirely filled with grout.

During loading, both tension sections and the compressive section of the anchor were simultaneously subjected to the applied load, working together to resist deformation. The performance of the composite anchor was evaluated by comparing it with tension anchors of different lengths, with the anchorage length of the composite anchor considered as an equivalent alternative to that of the tension anchor. Each group included three parallel samples, resulting in a total of 12 anchors. The parameters of the anti-floating anchors are presented in Table 2. All anchor holes had a diameter of 200 mm and were spaced 3 m apart. These holes were formed using an anchor-forming machine. Figure 3 illustrates the arrangement and physical depiction of the anti-floating anchors on the construction site. The anchor body of the floating anchors was constructed using a 40 mm diameter rebar (HRB 400) with a modulus of elasticity of 200 GPa, a density of 7850 kg·m^{-3}, and a Poisson's ratio of 0.3. After grouting, the floating anchors were cured for 28 days before conducting field load tests.

Table 2. Parameters of anti-floating anchors.

Anchor Name	Group Number	Anchor Number	Length of Bearing Section 1 # (mm)	Length of Bearing Section 2 # (mm)	Length of Pressure Section (mm)
composite anchor	group 1	K-6-1	750	750	1500
		K-6-2	750	750	1500
		K-6-3	750	750	1500
tension anchor	group 2	K-9-1	3000	/ [1]	/
		K-9-2	3000	/	/
		K-9-3	3000	/	/
tension anchor	group 3	K-11-1	4000	/	/
		K-11-2	4000	/	/
		K-11-3	4000	/	/
tension anchor	group 4	K-12-1	5000	/	/
		K-12-2	5000	/	/
		K-12-3	5000	/	/

[1] / indicates that this type of anchor does not exist in this unit anchoring section.

The loading monitoring device utilized in the experiment is depicted in Figure 4. The test program consists of a graded load, where a load of 85 knuckles is applied at each stage and maintained for a stable period of 5 min. The loading process employed a 100 T automatic oil pump and a hollow jack, with the loading value read using an intelligent pressure gauge. Tests of distance were conducted using a 100 mm mechanical percentage meter, placed on both sides of the anchor head. Deformation gages were strategically positioned, as illustrated in Figure 5. These gauges were evenly distributed across each anchorage section, with the ones in the tensile section affixed to the surface of the steel reinforcement, and those in the compressive section attached to the surface of the steel casing (as the axial force of the anchor body remains constant in the compressive section). To monitor strain changes on both sides of the bearing plate, deformation gages were applied on each side. Additionally, a static strain gauge was employed for strain data collection.

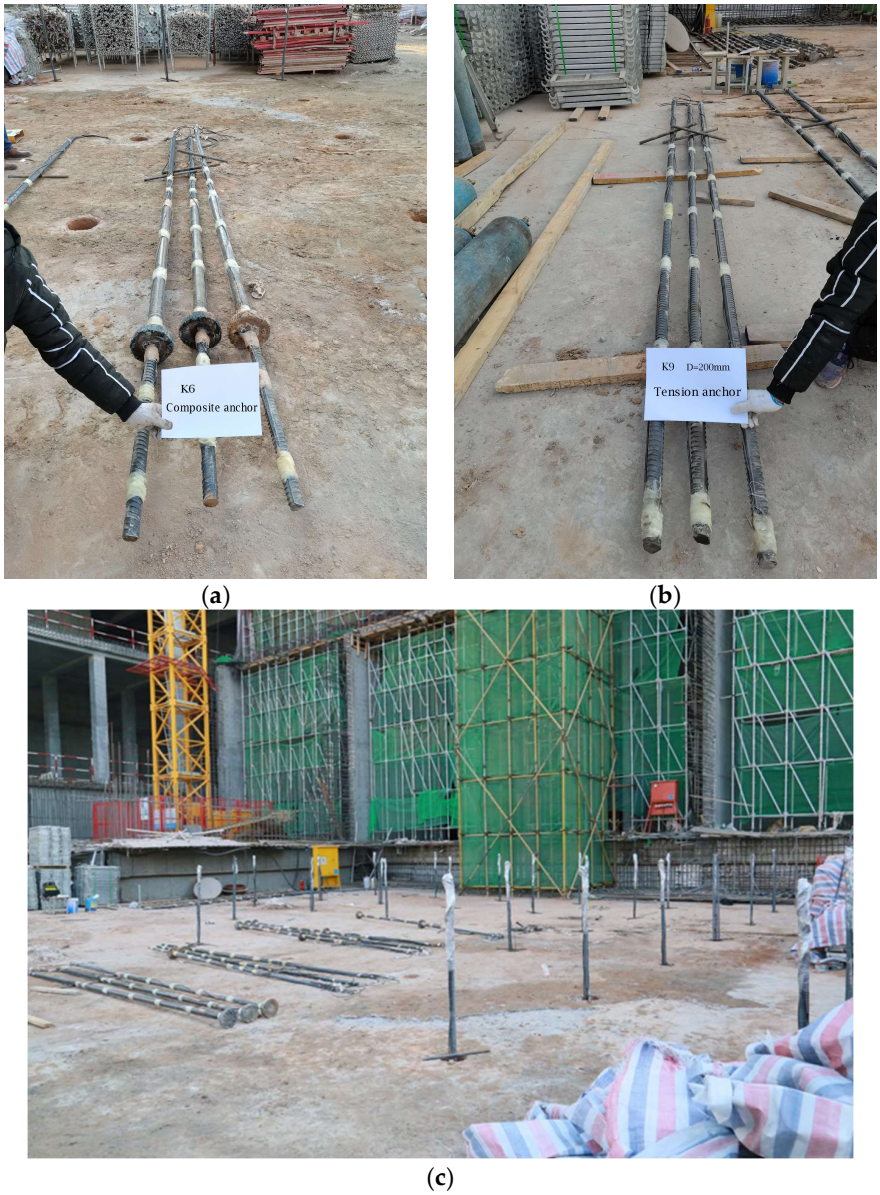
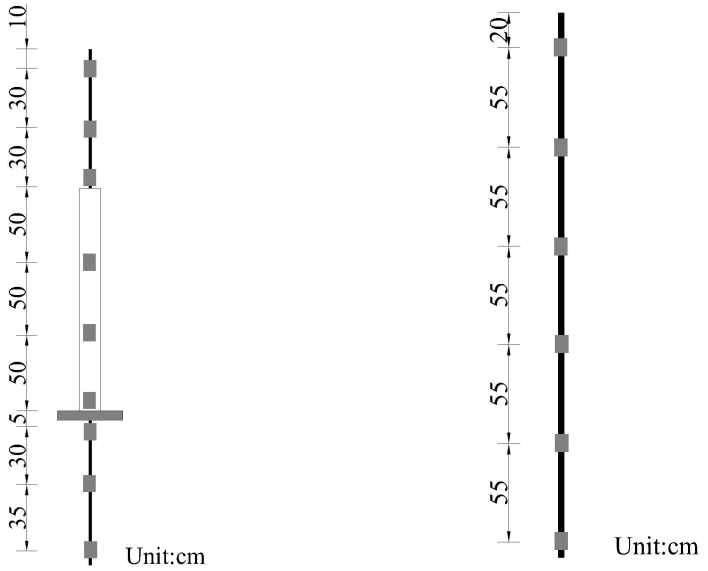


Figure 3. Field test anchors: (**a**) composite anchor; (**b**) tension anchor; (**c**) anchor arrangement.



Figure 4. Load and monitoring device.



(**a**) (**b**)

Figure 5. Strain gauge position of anchors: (**a**) composite anchor; (**b**) tension anchor.

During the test, strains at different anchorage depths of the anchors were measured, and the axial force distribution curves of the anchors were determined using Equation (1). In the equation, the compressive axial force is represented by "−" and the tensile axial force by "+", ensuring a clear distinction between the two.

$$N_{ij} = E_s A_{si} \varepsilon_{ij} + E_c A_{ci} \varepsilon_{ij} \quad (1)$$

Equation (1) is defined as follows: N_{ij} represents the axial force at the first interface of the anchor under load. E_s is the modulus of elasticity of the anchor body or steel casing, and A_{si} is the cross-sectional area of the anchor body or steel casing at the i-th section. ε_{ij} denotes the strain at the i-th section of the anchor under j-th load, E_c represents the modulus of elasticity of the grout body, and A_{ci} is the cross-sectional area of the grout body at the i-th section of the anchor. The impact of the anchor's weight on its axial force is minor, and is disregarded during the calculation process.

Axial force is determined according to Equation (1). The axial force at two measuring points is subtracted and divided by the cross-sectional area to determine the lateral friction resistance of the anchor. The calculation formula is given as Equation (2). To facilitate distinction, the compressive side frictional resistance is designated "−", and the tensile side frictional resistance is designated "+".

$$f_i = (N_i - N_{i-1}) / \pi D \Delta L \quad (2)$$

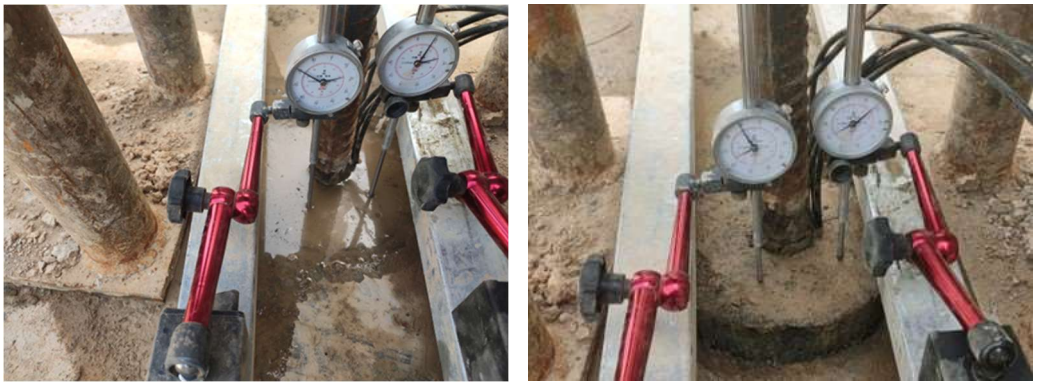
where N_i is the axial force at the i-th cross-section of the anchor (kN); N_{i-1} is the axial force at the i-th cross-section of the anchor (kN); D is the anchor diameter, D = 200 mm; and ΔL is the distance between two sections.

3. Results

3.1. Failure Characteristics of Anchors

Anchor failure can be classified as one of four types based on different causes: insufficient tensile strength, resulting in fracture of the anchor body; low mortar strength, leading to shear failure at the interface between the anchor body and grouting; weak soil or rock mass strength, causing conical pull-out failure where the anchor is extracted in a conical shape from the surrounding soil or rock mass; and shear failure occurring at the interface

between the soil or rock and the grouting material [34,35]. In the conducted experiment, shear failure at the second interface, specifically at the interface between the soil or rock mass and the grouting material, was observed in both the composite anchor and the 3 m, 4 m tension anchors. Conversely, the failure of the 5 m tension anchor was attributed to steel yielding, whereby the ultimate bearing capacity exceeded the limited tensile strength of the anchor body. The anchor failure diagram is depicted in Figure 6.



(**a**) (**b**)

Figure 6. Damage shape of anti-floating anchors: (**a**) primary loading; (**b**) pull-out failure.

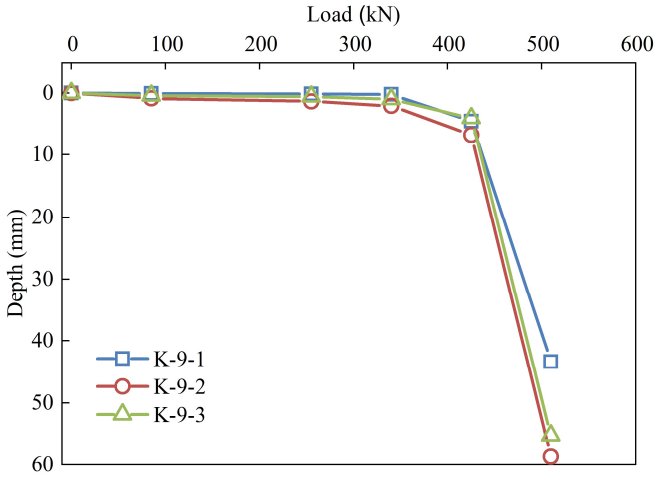
Upon application of the load, the cushion layer experiences a reaction force from the support system, and as depicted in Figure 6a, the groundwater present beneath the cushion layer continuously seeps out from the anchor hole under pressure. Once the anchor reaches its ultimate bearing capacity, the second interface undergoes failure, resulting in a significant reduction in the anchor's bearing capacity. Consequently, the load acting on the cushion layer diminishes, causing the groundwater to reverse its flow and either return to the lower portion of the cushion layer or infiltrate the lower region of the anchoring section through the second interface of the anchor, rather than continuing to seep out from the anchor hole. This phenomenon serves as a crucial criterion for determining the occurrence of anchor failure.

3.2. Load–Displacement Characteristics

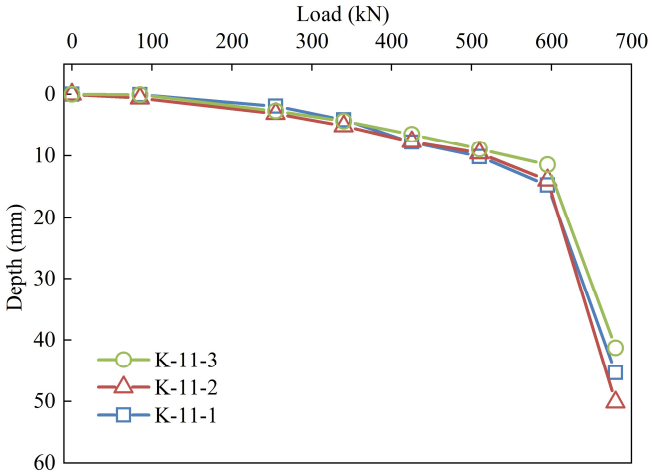
The load–displacement curve of the test anchor is illustrated in Figure 7. The data collection for composite anchor K-6-3 was incomplete due to construction damage during the experiment. Nonetheless, complete data were obtained for the remaining two anchors, as well as for the three tension anchors. The load–displacement curves for all anchors are presented in Figure 7. The anchor failure load, maximum displacement, and failure mode are summarized in Table 3.

The average ultimate bearing capacities for anchors K-6, K-9, and K-11 were determined as 675, 470, and 611.5 kN, respectively. Notably, anchor K-12 experienced tension-induced rupture, with its ultimate bearing capacity exceeding the ultimate tensile strength value of the anchor body at 715 kN. The ultimate bearing capacity of the composite anchor was 1.44 times that of tension anchor K-9, and 1.1 times that of tension anchor K-11. However, it was lower than the ultimate bearing capacity of tension anchor K-12.

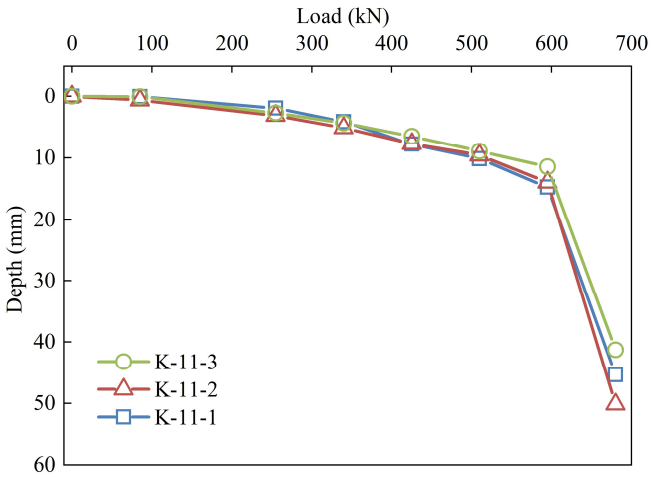
By incorporating a steel sleeve and a bearing plate in the middle section of the anchor body via welding, the ultimate bearing capacity of the composite anchor can be effectively enhanced. As a result, its ultimate bearing capacity surpasses that of tension anchors with the same anchorage length, as well as those with an anchorage length of 4 m.



(**a**)

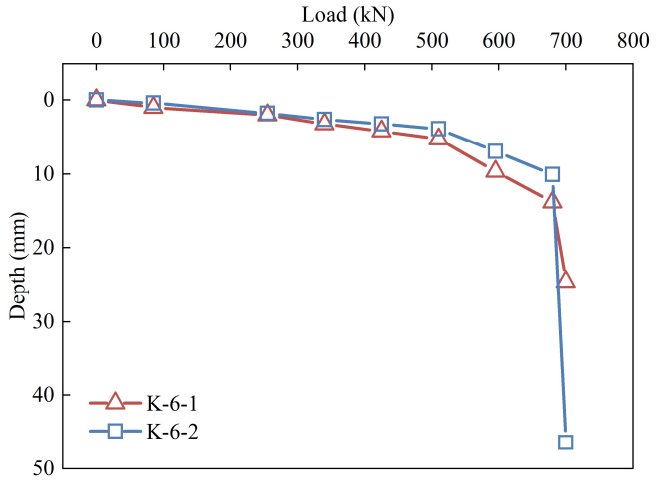


(**b**)

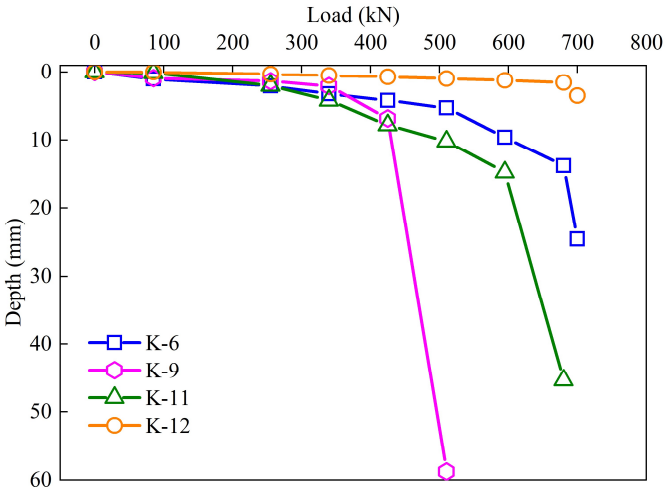


(**c**)

Figure 7. *Cont.*



(**d**)



(**e**)

Figure 7. Load and displacement relationship of anchor: (**a**) K-9; (**b**) K-11; (**c**) K-12; (**d**) K-6; (**e**) total displacement diagram.

The analysis of anchor head displacement during the failure of the four anchor groups reveals important insights. For anchor K-9, the average anchor head displacement before failure was 14.9 mm. Throughout each loading stage, the displacement of the anchor head consistently increased, demonstrating notable deformation and a strong capacity to adapt to deformation. Similarly, anchor K-11 exhibited an average anchor head displacement of 13.4 mm before failure, with displacement increments comparable to anchor K-9. In contrast, anchor K-12 displayed an average anchor head displacement of 5 mm before failure, with significantly smaller displacement increments compared to both anchor K-9 and K-11.

It was observed that as the anchor length increased, the ultimate bearing capacity of the tension anchor also increased. However, the displacement increments under each loading stage gradually decreased. On the other hand, the composite anchor demonstrated an average anchor head displacement of 13.01 mm before failure. Despite achieving an ultimate bearing capacity 1.44 times and 1.1 times greater than the K-9 and K-11 tension anchors, respectively, the composite anchor maintained substantial displacement under each loading stage. This indicates that the composite anchor exhibits enhanced structural ductility while simultaneously improving the ultimate bearing capacity [36].

Table 3. Results of anchor tests.

Anchor Name	Group Number	Anchor Number	Failure Load (kN)	Maximum Displacement (mm)	Destruction Form
composite anchor	group 1	K-6-1	670	13.59	Second interface failure
		K-6-2	680	12.43	Second interface failure
tension anchor	group 2	K-9-1	480	14.96	Second interface failure
		K-9-2	460	15.68	Second interface failure
		K-9-3	470	14.32	Second interface failure
tension anchor	group 3	K-11-1	610	14.76	Second interface failure
		K-11-2	605	13.98	Second interface failure
		K-11-3	620	11.43	Second interface failure
tension anchor	group 4	K-12-1	>715	3.44	Anchor damage
		K-12-2	>715	4.57	Anchor damage
		K-12-3	>715	6.91	Anchor damage

Figure 7e presents the comprehensive load–displacement curves for the four groups of anchors. The figure reveals interesting observations: when the anchor head load is below 255 kN, the composite anchor exhibits larger displacements compared to the tension anchor at the same load level. However, as the load surpasses 255 kN, the anchor head displacement of the composite anchor gradually becomes smaller than that of tension anchors of the same length. Furthermore, under equivalent load levels, the anchor head displacement of the composite anchor is smaller than that of the K-9 and K-11 tension anchors. This behavior can be attributed to the ability of the composite anchor's compression section to transfer the load to a deeper rock and soil foundation. During the initial load-bearing stage, the composite anchor demonstrates better deformation adaptability. In the later load-bearing stage, the compression section experiences radial deformation under pressure, effectively preventing sudden anchor head displacement.

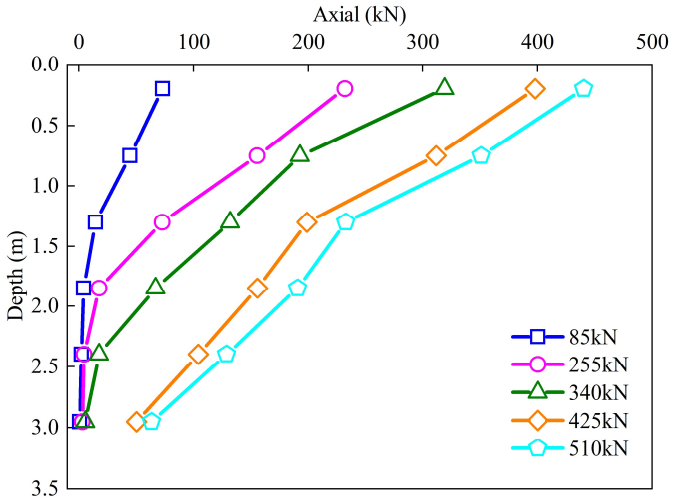
As is apparent from Figure 7a–c, the load–displacement curves for tensile anchor rods display a two-stage distribution. If the applied load is below the anchor rod's ultimate pullout capacity, displacement increases gradually, while the load-carrying capacity rises rapidly. As the failure load is approached, a noticeable trend of a slower increase in load becomes apparent, and the displacement exhibits a sharp and distinctive steep rise. This similarity aligns with the findings of Wu et al. [37] and Huang et al. [38] for tensile-type anchors, but differs from the recent results of GFRP anchors. According to Kou et al. [8], this phenomenon is attributed to the elastic modulus of the anchor material. On the other hand, the load–displacement curve of the composite anchor exhibits small slope changes before and after failure, with slow displacement increase post-failure, indicating that it still maintains a certain bearing capacity. Consequently, as an engineering anchor, the composite anchor demonstrates superior deformation adaptability, and its failure exhibits a certain level of predictability.

3.3. Axial Force Distribution

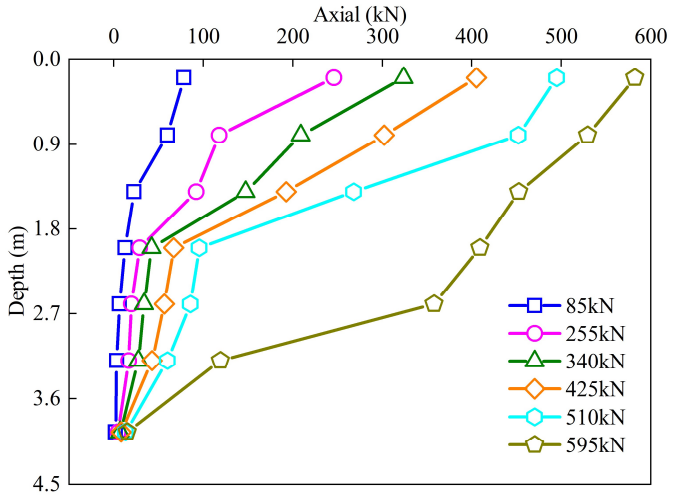
Figure 8 displays the distribution of axial force along the depth of the anchor. The axial force of the tension anchor exhibits a gradual decrease as the depth of anchorage increases, eventually approaching zero at the end of the anchorage section. The axial force of the tension anchor for depth can be divided into two sections among the three groups. When the anchorage depth is less than 2 m, the axial force decays slowly, whereas for depths exceeding 2 m, the axial force decays rapidly. It is observed that an anchorage length of 2 m represents the optimal effective length for tension anchors. Thus, it is recommended to limit the length of each anchorage unit to not exceed 2 m. Although the ultimate load-carrying capacity of the tension anchor gradually increases with the anchorage length, the overall pattern of axial force distribution remains relatively unchanged. Extensive experimental research and theoretical analysis on anchor load transfer mechanisms have

further validated this assertion [38–40]. In examining Figure 9b,c together, it is evident that in the case of this load-concentrating anchor under tension, the distribution of bond stresses between the grout and the surrounding soil or rock varies significantly along the length of the anchor section [41]. The shorter the anchor section of the anchor, the greater the average bond strength. The effective length of the anchor section that utilizes the shear strength of the soil or rock is constrained. Therefore, in this experimental process, the length of the anchor section units was set at 2 m to ensure the optimal utilization of the soil or rock strength in each rod unit's anchor section.

The axial force variation curve of the composite anchor to anchorage depth can be divided into three distinct sections. The axial force at the tensile Sections 1 # and 2 # gradually decreases as the anchorage depth increases, while the axial force at the compression section gradually increases. This discrepancy in axial force distribution between the compression section and the tension anchor is attributed to the absence of bonding between the anchor body and the grout. As a result, the axial force of the anchor body does not decay in the compression section, and the load is effectively transferred to the bearing plate and the upper and lower anchorage sections. Despite this difference, the overall pattern of axial force distribution in the composite anchor follows a similar trend to that of the tension anchor, exhibiting a gradual reduction as the distance from the load-bearing end increases.

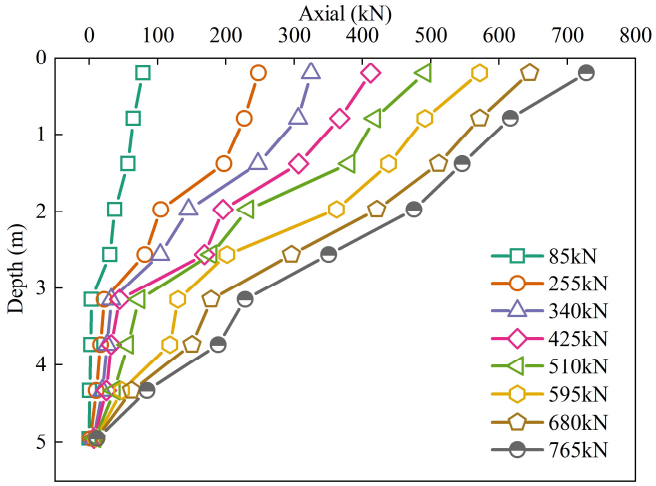


(**a**)

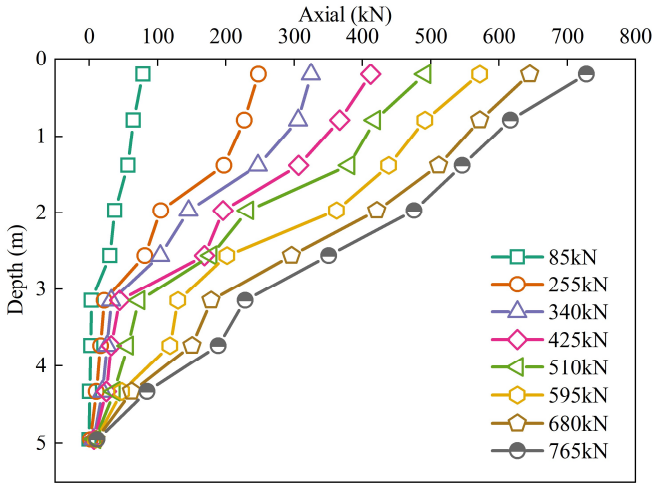


(**b**)

Figure 8. *Cont.*

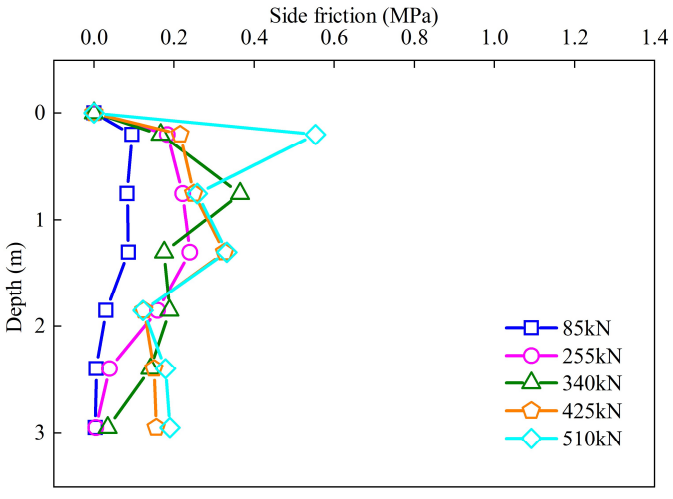


(**c**)



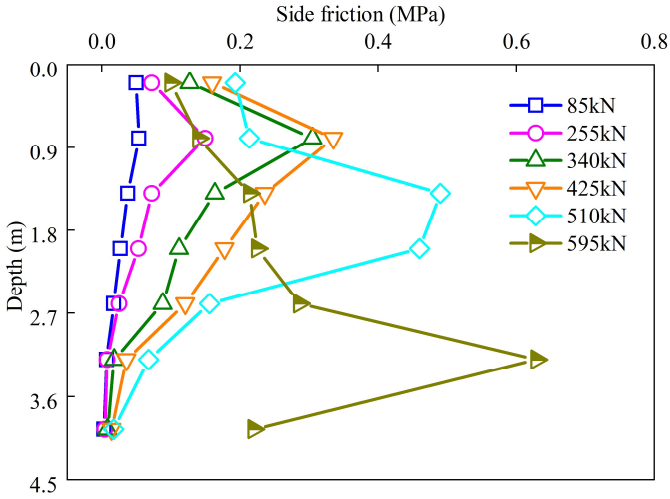
(**d**)

Figure 8. Distribution for axial force: (**a**) K-9; (**b**) K-11; (**c**) K-12; (**d**) K-6.

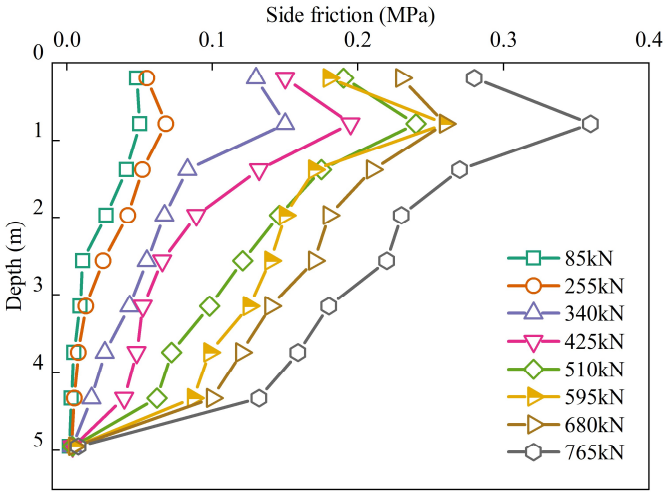


(**a**)

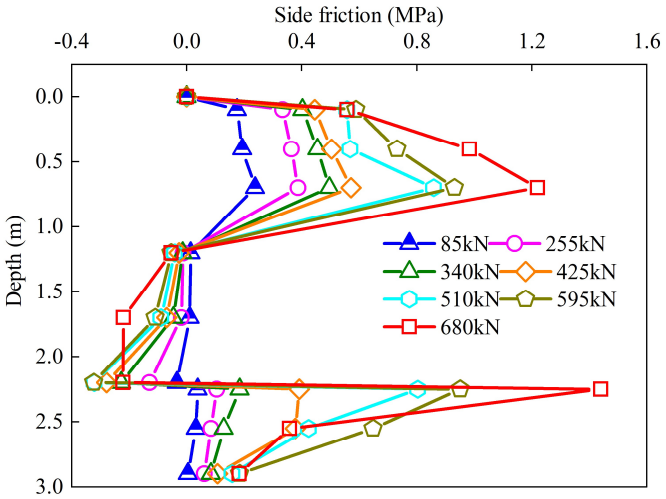
Figure 9. *Cont*.



(**b**)



(**c**)



(**d**)

Figure 9. Distribution for side friction resistance: (**a**) K-9; (**b**) K-11; (**c**) K-12; (**d**) K-6.

As depicted in Figure 8d, it is observed that when the composite anchor bears a load of less than 255 kN, the end of the bearing section experiences tension rather than compression.

This occurrence can be attributed to the relatively low pressure exerted on the bearing plate, causing the axial force to gradually decrease as it moves away from the plate. Consequently, at the end of the bearing section, the pressure diminishes, and the upper bearing Section 1 # (refer to Figure 1) comes into play. This transition leads to a shift in the anchorage section from a state of compression to tension [42]. With a further increase in the anchor head load, the entire bearing section enters a pressurized state. Notably, at the junction of the tensile Section 1 # and the compressive section, the anchorage section experiences a combination of tension and compression forces, necessitating careful consideration during the design and construction of the anchor.

At a load of 340 kN (with no damage to any of the four anchor sets), the load per unit anchorage length was analyzed for the lower anchorage section of the tension and composite anchors. The load per unit anchorage length in the lower section for anchors K-6, K-9, K-11, and K-12 was determined to be 113.5, 29.7, 34, and 28.8 kN, respectively. Notably, the load per unit anchorage length in the lower section of the composite anchor was significantly higher than that of the three tension anchor sets. This finding indicates that the welded bearing plate and steel casing in the middle of the anchor effectively facilitate the transfer of the anchor head load to the underlying geotechnical body. The composite anchor demonstrates enhanced utilization of strength in the lower part of the anchorage section, thereby shifting the critical anchorage depth of the anchor downward.

3.4. Side Friction Distribution

As shown in Figure 9, the graph illustrates the distribution of side friction resistance along the depth of the anchor. The side friction resistance of the anchor rod gradually decreases as the anchoring depth increases. While the upper anchoring segment of the anchor fully utilizes its lateral friction resistance, the lower anchoring segment experiences insufficient lateral friction resistance. This deficiency results in local stress concentration in the upper anchoring section, leading to premature failure in that area and subsequently extending to the lower anchoring section, causing overall anchor failure. The lateral frictional resistance of the upper and lower anchoring sections of the anchor cannot effectively function simultaneously. By analyzing the effective lateral frictional resistance of three sets of tensioned anchors, it was determined that the maximum lateral frictional resistance of anchors K-9, K-11, and K-12 is 0.4, 0.3, and 0.27 MPa, respectively. Although the ultimate bearing capacity of the tensioned anchor increases with anchor length, the degree of lateral frictional resistance decreases.

As shown in Figure 9d, The lateral friction resistance of the composite anchor exhibits a three-stage distribution. The absolute values of lateral friction resistance for all three anchor units exceed 0.3 MPa, with the lateral friction resistance on the bearing Section 1 # side reaching 0.6 MPa or higher. In the pressure-bearing section and the two-unit anchorage section of the tension-bearing section, the absolute value of lateral frictional resistance is approximately 0.4 MPa, with the highest value observed. The peak value of lateral frictional resistance gradually increases with increasing load for both composite anchors and tension anchors, while the position of the peak value remains relatively constant. As the load increases, the lateral frictional resistance gradually extends downward along the depth distribution [43].

The lateral frictional resistance of the lower anchorage section of the tensioned anchor is consistently lower than that of the lower anchorage section of the composite anchor, and the degree of lateral frictional resistance decreases with increasing anchorage length. The overall degree of lateral frictional resistance exerted by the three anchoring units in a composite anchor is higher than that of a tension anchor, resulting in a larger range of lateral frictional resistance. This is attributed to the shorter length of each anchoring segment, which reduces the bond softening effect and enables more effective utilization of the soil strength within the anchoring segment, consequently improving the ultimate bearing capacity of the anchor [7].

The lateral friction resistance proves equally effective in the anchored sections of the compression section and the tension section, as the load transmitted to these sections is evenly distributed by the bearing plate to both sides. This effectively prevents local stress concentration, facilitates more efficient utilization and uniform distribution of the lateral friction resistance of the anchor, and serves as a key factor in enhancing the ultimate bearing capacity of the composite anchor.

4. Discussion

The research for traditional tension (pressure)-type anchors has reached a high level of maturity [44–46]. Nevertheless, with the continuous advancement of underground engineering, conventional anchors are confronted with challenges such as load concentration effects and constraints imposed by critical anchoring depths. These limitations make them unsuitable for addressing the demands of modern complex geological conditions and engineering prerequisites. As a consequence, novel anchor designs have been continually introduced.

To address the issue of load concentration in traditional anchors, Tu et al.'s research [23,47,48] suggests incorporating pressure plates to segment the anchor unit into pressure-anchor and tension-anchor sections. This segmentation allows the load to be divided into smaller components, acting on the pressure-anchor and tension-anchor sections separately. Presently, tension–compression-dispersed composite anchors have been applied in practical contexts, such as the Chongqing International Metropolitan Project, the Lifan Center-LFC Project, and the Yunnan Xianglin Highway Project [49–51]. Field monitoring data indicate that in comparison with conventional tension anchors, the tension–compression composite anchor structure displays a shorter period for anchor stress stabilization after tensioning. This demonstrates superior load-holding capabilities, with minimal load loss amounting to less than 7% of the total load. Tension–compression-dispersed anchors deliver dependable anchoring results and a more rational load distribution [51]. As depicted in Figure 8, our proposed innovative tension–compression-dispersed composite anchor demonstrates a distinctive three-segment distribution, transmitting loads from the lower anchor head to the upper and lower load-bearing segments. This load distribution strategy effectively divides the load into three distinct portions. During practical experiments, variations in local rock hardness can result in oversized borehole diameters occurring during anchor hole drilling. Furthermore, the presence of a bearing plate on the anchor affects the anchor's descent into the borehole. Consequently, vertical adjustments are necessary to ensure the anchor is correctly positioned within the borehole. This situation can impact the anchor's construction progress and may result in a modest increase in construction costs.

The results presented in Figure 9a,d reveal that for a load of 510 kN, the peak shear stress at the interface of a conventional tension-type anchor is 0.55 MPa. In contrast, the tension–compression-dispersed composite anchor displays a higher peak shear stress of 0.86 MPa. Surprisingly, the tension–compression-dispersed composite anchor exhibits an increased interface shear stress compared to the traditional tension-type composite anchor, in contrast to the findings in Refs. [23,46]. This discrepancy can be attributed to the placement of the pressure section between pressure Sections 1 # and 2 #. In this configuration, the grout within the pressure section is subjected to compression, leading to lateral expansion and thereby enhancing interface frictional resistance within a defined range [48,52]. This phenomenon amplifies the normal stress and subsequently augments the interfacial shear strength.

However, despite efforts to reduce the anchoring lengths of individual units by adding load-bearing plates [23], which ensures that each unit's anchoring length remains within the critical anchoring range and leads to a more uniform distribution of shear stress, practical underground engineering often involves heterogeneous geological conditions and factors like water ingress. Research by Kim et al. [53] indicates that when rock masses are exposed to water infiltration, the anchoring performance of anchors is significantly compromised.

Under these circumstances, the distribution of loads achieved by the tension–compression-dispersed composite mechanism cannot be solely determined using the strength of the rock mass. Therefore, novel anchor designs based on the stratification of rock formations hold promise for enhancing the ultimate load-bearing capacity of anchors and ensuring the stability of upper-level structural elements in complex geological environments.

Current research [54–57] has developed comprehensive theoretical models for traditional fully bonded anchors. However, due to the presence of pressure segments, the load transmission mechanism of tension–compression-dispersed composite anchors deviates from that of traditional tension-type anchors. As a result, the aforementioned theories cannot be directly applied to the theoretical analysis of these novel anchors. In our study, full-scale field tests were conducted on tension–compression type discrete anti-floating anchors. The test phenomena were analyzed, and a simplified theoretical model (Figure 10) and numerical simulations of composite anchors were proposed. Based on the critical anchor length of traditional anchors, the reasonable anchor length and bearing ratio of composite anchors were determined [23]. The difference in plastic zone between traditional anchors and composite anchors was investigated [58]. During model development, existing theories were not integrated, and a comprehensive model suitable for tension–compression-dispersed composite anchors has not yet been constructed. Consideration can be given to the research related to axial vibration (both tension and compression) of rod-like elements based on the advanced theories of elasticity [59–64], taking into account existing interface bonds and end-plates when modeling a composite anchored in cement grout. It is crucial in the future to develop a theoretical model capable of calculating the effective anchorage length of composite anchors. This model will serve as a valuable reference for anchor design, construction, and standardization. Furthermore, it is necessary to develop a theoretical model for load transmission in anchors based on existing experimental parameters. This model will facilitate the proposal of reasonable safety factors for anchor design, ensuring the economic viability and reliable safety of composite anchors in practical use. Given the multitude of factors involved in the current technical challenge, encompassing the mechanical properties of rock anchors and sleeve steel, concrete grout, interface bonds for both Interface #1 and Interface #2, as well as the geometrical properties of both the grout and anchor, calculating the axial load-bearing capacity of tension–compression composite anchors could be a formidable undertaking. To address this challenge, the creation of a comprehensive analytical or numerical model [65,66] coupled with the incorporation of deep learning [67–69] and artificial intelligence [70,71] would prove highly beneficial. This will aid in further complementing and refining the theoretical foundation of these innovative structural anchors.

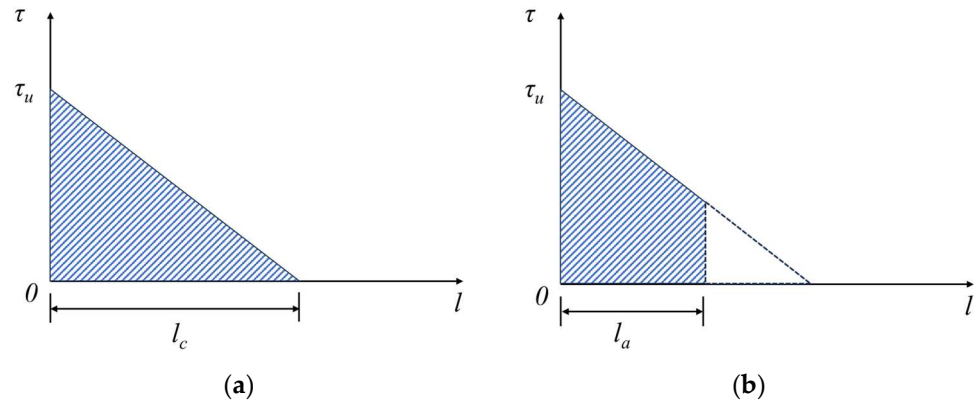


Figure 10. Simplified model for shear stress along anchorage length: (**a**) a tension-type anchor; (**b**) the distribution of interface shear stress τ_u when the anchorage length l_a is less than the critical anchorage length l_c [23].

5. Conclusions

This study is a comparative analysis of the anchorage performance of tension anchors and composite anchors through field tests. The following conclusions were drawn:

(1) The ultimate bearing capacity of a 3 m composite anchor is 1.44 times that of a tension anchor of the same length, and 1.1 times that of a 4 m tension anchor. Unlike tension anchors that rely on increasing anchorage length to enhance bearing capacity, the composite anchor improves bearing capacity effectively by incorporating structural modifications.

(2) The composite anchor not only improves ultimate bearing capacity, but also exhibits significant deformation during the early loading stage. It effectively prevents sudden displacement increases in the anchor head in the later loading stage, and the load–displacement curve shows a small slope before and after failure.

(3) The axial force transmission behavior of tension anchors with different anchorage lengths was analyzed in this experiment. It was observed that the axial force of the three groups of tension anchors experienced abrupt changes at an anchorage depth of approximately 2 m, with an increased attenuation rate. Therefore, in the design of load-dispersed composite anchors, it is recommended to keep the effective anchorage length of each unit anchorage section below 2 m to fully utilize the strength of the rock and soil mass in the anchorage section.

(4) By implementing structural measures such as a bearing plate and steel casing, the tension–compression-dispersed composite anchor enables load transmission to deeper rock and soil masses, fully utilizing the strength of the lower rock and soil mass. It effectively prevents bond-weakening effects, reduces local stress concentration to some extent, achieves a more uniform distribution of side friction resistance, and enhances the overall anchorage performance of the anchor.

Author Contributions: Y.L.: Conceptualization, Methodology, Field test. K.X.: Structure design of anchors, Field test, Writing—original draft. B.W.: Formal analysis, Writing—review and editing. J.L.: Investigation, Field test. Y.M.: Field test. M.Z.: Conceptualization, Methodology, Funding acquisition. All authors have read and agreed to the published version of the manuscript.

Funding: This research received no external funding.

Institutional Review Board Statement: Not applicable.

Informed Consent Statement: Not applicable.

Data Availability Statement: The data presented in this study are available on request from the corresponding author. The data are not publicly available due to we are currently conducting further numerical simulation work to further reveal the mechanism of the anchor. The data can be published until we have done all simulation study.

Acknowledgments: Thanks to the staff involved in the anchor bolt pull-out test for their contributions. Additionally, appreciation is extended to Zhou Zhixiong, Zhang Ruiling and Zang Yang, Wang Chengfu from Lanzhou University of Technology for their insightful suggestions in revising this article.

Conflicts of Interest: Authors Yuguo Liu, Ji Le and Yanqing Ma were employed by the company China Construction Fourth Engineering Bureau Co. The remaining authors declare that the research was conducted in the absence of any commercial or financial relationships that could be construed as a potential conflict of interest.

References

1. Guang, C.; Rui, W.; Mu, Z.; Jing, S.; Yang, Y.; Xiao, Z. Present situation and developmental trend of urban underground space development and utilization in China. *Earth Sci. Front.* **2019**, *26*, 39.
2. Li, X.; Li, C.; Parriaux, A.; Wu, W.; Li, H.; Sun, L.; Liu, C. Multiple resources and their sustainable development in Urban Underground Space. *Tunn. Undergr. Space Technol.* **2016**, *55*, 59–66. [CrossRef]
3. Tan, Z.; Roberts, A.C.; Christopoulos, G.I.; Kwok, K.-W.; Car, J.; Li, X.; Soh, C.-K. Working in underground spaces: Architectural parameters, perceptions and thermal comfort measurements. *Tunn. Undergr. Space Technol.* **2018**, *71*, 428–439. [CrossRef]

4. Mothersille, D.; Littlejohn, S. Grouting of anchors to resist hydrostatic uplift at Burnley tunnel, Melbourne, Australia. In Proceedings of the Grouting and Deep, Mixing 2012, Engineers, New Orleans, LA, USA, 15–18 February 2012; pp. 1073–1084.
5. Zheng, C.; Bai, X.; Zhang, M.; Wang, H. Research progress on glass fiber reinforced polymer anchors in anti-floating engineering of underground structures. *Mater. Rep.* **2020**, *34*, 13194–13202.
6. Dong, C.; Zheng, Y.-R.; Chen, X.; Tang, X. Research on composite support pattern of soil nails and prestressed anchors in deep foundation pits. *Rock Soil Mech.* **2009**, *30*, 3793–3796.
7. Hyett, A.; Moosavi, M.; Bawden, W. Load distribution along fully grouted bolts, with emphasis on cable bolt reinforcement. *Int. J. Numer. Anal. Methods Geomech.* **1996**, *20*, 517–544. [CrossRef]
8. Kou, H.; Guo, W.; Zhang, M. Pullout performance of GFRP anti-floating anchor in weathered soil. *Tunn. Undergr. Space Technol.* **2015**, *49*, 408–416. [CrossRef]
9. Sun, S.; Lu, Y. Rock & Soil Anchoring Technology and Its Engineering Application. In Proceedings of the 2017 2nd International Conference on Environmental Science and Energy Engineering (ICESEE 2017), Beijing, China, 15–16 January 2017.
10. Jian, Y.; Wen, J.; Huang, W. Pull-out test and ultimate bearing capacity calculation of grouting branch-type anchor. *Rock Soil. Mech.* **2021**, *42*, 1126–1132.
11. Wei, H.; Jian, B.; Yang, J.; Dou, H.; Lou, J. Prototype test and load transfer characteristic analysis of multi-disk anchor rod. *Rock Soil. Mech.* **2023**, *44*, 520–530.
12. Zhang, Y.; Bai, X.; Yan, N.; Sang, S.; Jing, D.; Chen, X.; Zhang, M. Load Transfer Law of Anti-Floating Anchor With GFRP Bars Based on Fiber Bragg Grating Sensing Technology. *Front. Mater.* **2022**, *9*, 849114. [CrossRef]
13. Sun, G.; Yan, N.; Bai, X.; Liu, J.; Hou, D.; Sang, S.; Zhang, M.; Wang, P.; Jing, D. Laboratory full-scale test on the bond property of GFRP anchor to concrete. *Constr. Build. Mater.* **2023**, *396*, 132216. [CrossRef]
14. Xiao, B.; Xue, L.; Mingyi, Z.; De, J.; Chen, Z. Field tests and load-displacement models of GFRP bars and steel bars for anti-floating anchors. *Acta Mater. Compos. Sin.* **2021**, *38*, 4138–4149.
15. Cheng, K. Present status and development of ground anchorages. *China Civ. Eng. J.* **2001**, *34*, 7–12.
16. Zhou, S.; Feng, S.; Dai, C.; Xu, Q.; Ke, Z. Model Test of Stress and Displacement of Recyclable Anchor Rod Support Structure. *Appl. Sci.* **2023**, *13*, 7713. [CrossRef]
17. Xue, W.; Gang, W.; Yu, J.; Bin, G.; Bo, L. Mechanism of CTC-yield bolts and its experimental research. *Chin. J. Geotech. Eng.* **2015**, *37*, 139–147.
18. Shen, Q.; Yuan, D.-R.; Chen, C.-X. A New Monitoring Device for the Force States of the Pressure Dispersed Anchor Cable. In Proceedings of the 5th International Conference on Advanced Engineering Materials and Technology (AEMT 2015), Guangzhou, China, 22–23 August 2015; pp. 836–841.
19. Jin, J.; Bing, T.; Hai, W.; Gang, M.; Da, Y. Mechanical behaviors of pressure-dispersive prestressed anchor. *Chin. J. Geotech. Eng.* **2011**, *33*, 1320–1325.
20. He, Z.; Xin, A. Prestress loss model and experimental study of anchor cables in soft soil area. *Adv. Mater. Res.* **2012**, *433*, 2769–2773. [CrossRef]
21. Shu, W.; Hong, F.; Yan, Z. Study on anchorage mechanism and application of tension-compression dispersive anchor cable. *Rock Soil Mech.* **2018**, *39*, 2155–2163.
22. Xiao, C.; Jiu, Z.; Peng, Z. Calculation and analysis of differential tension of pressure dispersion anchor cables at Lianghekou hydropower station. *Explor. Eng.* **2020**, *47*, 85–88.
23. Bing, T.; Shi, L.; Jin, Y.; Jing, H.; Jian, Z.; Jin, J. Analysis of anchorage performance on new tension-compression anchor: I simplified theory. *Chin. J. Geotech. Eng.* **2018**, *40*, 2289–2295.
24. Killic, A.; Yasar, E.; Atis, C. Effect of bar shape on the pull-out load capacity of fully grouted rock bolt. *Tunn. Undergr. Space Technol.* **2002**, *18*, 1–6. [CrossRef]
25. Serrano, A.; Olalla, C. Tensile resistance of rock anchors. *Int. J. Rock Mech. Min. Sci.* **1999**, *36*, 449–474. [CrossRef]
26. Li, C.C.; Kristjansson, G.; Høien, A.H. Critical embedment length and bond strength of fully encapsulated rebar rockbolts. *Tunn. Undergr. Space Technol.* **2016**, *59*, 16–23. [CrossRef]
27. Rui, G.; Wen, C.; Jian, D. Pullout mechanical analysis of soil anchor based on softening behavior of interface. *J. Cent. S. Univ.* **2012**, *43*, 4003–4009.
28. Małkowski, P.; Feng, X.; Niedbalski, Z.; Żelichowski, M.J.R.M.; Engineering, R. Laboratorial Tests and Numerical Modeling of Rock Bolts Bonded by Different Materials. *Rock Mech. Rock Eng.* **2023**, *56*, 2589–2606. [CrossRef]
29. Zheng, J.; Dai, J. Analytical solution for the full-range pull-out behavior of FRP ground anchors. *Constr. Build. Mater.* **2014**, *58*, 129–137. [CrossRef]
30. Klar, A.; Nissim, O.; Elkayam, I. A hardening load transfer function for rock bolts and its calibration using distributed fiber optic sensing. *J. Rock Mech. Geotech. Eng.* **2023**, *15*, 2816–2830. [CrossRef]
31. Zhang, Y.; Zhao, H.; Zhang, X. Test study of mechanical performances of anchorage zone of pressure dispersion anchor cable style. *Chin. J. Rock Mech. Eng.* **2010**, *29*, 3052–3056.
32. Liu, X.; Li, Z.; Tai, P.; Chen, R.; Fu, W. In-situ Experimental Investigation on Stress Distribution of Grout Body of Tension-type Ground Anchor. *Chin. J. Undergr. Space Eng.* **2021**, *17*, 63–70.
33. Ostermayer, H.; Scheele, F. Research on ground anchors in non-cohesive soils. *Rev. Française Géotechnique* **1978**, *3*, 92–97. [CrossRef]

34. Grindheim, B.; Aasbø, K.S.; Høien, A.H.; Li, C.C. Small block model tests for the behaviour of a blocky rock mass under a concentrated rock anchor load. *Geotech. Geol. Eng.* **2022**, *40*, 5813–5830. [CrossRef]
35. Littlejohn, G.S.; Bruce, D.A. Rock anchors-state of the art. Part 1: Design. *Ground Eng.* **1975**, *8*, 25–32.
36. Zhang, Y.; Li, L.; Xiao, R. Model test research on mechanical behavior of compression type rock bolt. *Rock Soil. Mech.* **2010**, *31*, 2045–2050.
37. Shu, W.; Yong, Z.; Kang, M. An analysis of working performance of pressure-type and tensile-type anchor. *Hydrogeol. Eng. Geol.* **2008**, *5*, 45–49.
38. Huang, M.; Zhou, Z.; Ou, J. Nonlinear full-range analysis of load transfer in fixed segment of tensile anchors. *Chin. J. Rock Mech. Eng.* **2014**, *33*, 2190–2199.
39. Liang, C.; Pei, Z.; Fan, W. Several mechanical concepts for anchored structures in rock and soil. *Chin. J. Rock Mech. Eng.* **2015**, *34*, 668–682.
40. Guo, Z.; Han, L.; Li, Y.; Hu, H.; Zhang, Y.; Luo, S. Analysis of Stresses on Wholly Grouted Anchors Based on Different Constitutive Models. *Geotech. Geol. Eng.* **2019**, *37*, 2495–2501. [CrossRef]
41. Xian, Z.; Da, L.; Shi, L.; Kui, Z.; Xiao, X.; Ningbo, D.U. Comprehensive research of critical anchorage length problem of rod of anchorage structure. *Chin. J. Rock Mech. Eng.* **2009**, *28*, 3609–3625.
42. Grindheim, B.; Li, C.C.; Høien, A.H. Full-scale pullout tests of rock anchors in a limestone quarry focusing on bond failure at the anchor-grout and grout-rock interfaces. *J. Rock Mech. Geotech. Eng.* **2023**, *15*, 2264–2279. [CrossRef]
43. Yue, Z.; Li, A.; Wang, P. An analytical analysis for the mechanical performance of fully-grouted rockbolts based on the exponential softening model. *Int. J. Min. Sci. Technol.* **2022**, *32*, 981–995. [CrossRef]
44. Anzanpour, S.; Aziz, N.; Remennikov, A.; Nemcik, J.; Mirzaghorbanali, A.; Rastegarmanesh, A. Laboratory study of the behaviour of grouted cable bolts under static and dynamic axial loading. In Proceedings of the Eurock 2022: Rock and Fracture Mechanics in Rock Engineering and Mining, Espoo, Finland, 12–15 September 2023.
45. Kömürlü, E.; Kesimal, A. Rock bolting from past to present in 20 inventions. *MT Bilimsel* **2016**, *9*, 69–85.
46. Purcell, J.; Vandermaat, D.; Callan, M.; Craig, P. Practical investigations into resin anchored roof bolting parameters. In Proceedings of the 16th Coal Operators' Conference.Mining Engineering, Wollongong, NSW, Australia, 10–12 February 2016; pp. 53–63.
47. Bing, T.; Jin, Y.; Jin, H.; Qiang, C.; Guo, X.; Jin, J. Analysis of anchorage performance on new tension-compression anchor II: Model test. *Chin. J. Geotech. Eng.* **2019**, *41*, 475–483.
48. Bing, T.; Yan, C.; Jin, H.; Jin, Y.; Guo, X.; Qiang, C. Analysis of anchorage performance on new tension-compression anchor III field test. *Chin. J. Geotech. Eng.* **2019**, *41*, 846–854.
49. Rui, C. Application of tension and compression dispersed anchor cables in landslide control on Xianglin Highway. *Chin. Foreign Entrep.* **2014**, 228–229. [CrossRef]
50. Xian, C. Study the Anchoring Stress Mechanism ofthe Tension-Compression Dispersed Anchor Cable. Master's Thesis, Chongqing University, Chongqing, China, 2015.
51. Yan, Z. Study on the Tension-Compression Dispersive Anchor Cable's Applicationto Building Rock Slope. Master's Thesis, Chongqing University, Chongqing, China, 2015.
52. Liu, J.; Wu, P.; Yin, H.; Zhong, D.; Li, S.; Zhou, H.; Li, Z.; Xu, H. Pressure-dispersive anti-float anchor technique and its application to engineering. *Chin. J. Rock Mechan Eng.* **2005**, *24*, 3948–3953.
53. Kim, H.; Kim, K.; Kim, H.; Shin, J. Anchorage mechanism and pullout resistance of rock bolt in water-bearing rocks. *Geomech. Eng.* **2018**, *15*, 841–849.
54. Liu, X.; Ma, Z. Mechanical behavior analysis of fully grouted bolt under axial load. *Sci. Rep.* **2023**, *13*, 421. [CrossRef]
55. Aghchai, M.H.; Maarefvand, P.; Rad, H.S. Analytically determining bond shear strength of fully grouted rock bolt based on pullout test results. *Period. Polytech. Civ. Eng.* **2020**, *64*, 212–222.
56. Jin, Z.; Peng, Z. Analytical model of fully grouted bolts in pull-out tests and in situ rock masses. *Int. J. Rock Mech. Min. Sci.* **2019**, *113*, 278–294.
57. Ren, F.; Yang, Z.; Chen, J.F.; Chen, W. An analytical analysis of the full-range behaviour of grouted rockbolts based on a tri-linear bond-slip model. *Constr. Build. Mater.* **2010**, *24*, 361–370. [CrossRef]
58. Yang, S.; Zhu, X.; Zhang, G.; Yang, L.; Xia, H.; Li, W. Research on the Mechanics Performance of the New Tension–Compression Rock Bolt Through Numerical Simulation. *Geotech. Geol. Eng.* **2022**, *40*, 2255–2266. [CrossRef]
59. Arda, M. Axial dynamics of functionally graded Rayleigh-Bishop nanorods. *Microsyst. Technol.* **2021**, *27*, 269–282. [CrossRef]
60. Kiani, K. Free dynamic analysis of functionally graded tapered nanorods via a newly developed nonlocal surface energy-based integro-differential model. *Compos. Struct.* **2016**, *139*, 151–166. [CrossRef]
61. Kiani, K. Nonlocal-integro-differential modeling of vibration of elastically supported nanorods. *Phys. E Low-Dimens. Syst. Nanostructures* **2016**, *83*, 151–163. [CrossRef]
62. Kiani, K.; Żur, K.K. Dynamic behavior of magnetically affected rod-like nanostructures with multiple defects via nonlocal-integral/differential-based models. *Nanomaterials* **2020**, *10*, 2306. [CrossRef]
63. Yuan, Y.; Xu, K.; Kiani, K. Torsional vibration of nonprismatically nonhomogeneous nanowires with multiple defects: Surface energy-nonlocal-integro-based formulations. *Appl. Math. Model.* **2020**, *82*, 17–44. [CrossRef]

64. Yuan, Y.; Zhao, K.; Zhao, Y.; Kiani, K. Nonlocal-integro-vibro analysis of vertically aligned monolayered nonuniform FGM nanorods. *Steel Compos. Struct.* **2020**, *37*, 551–569.
65. Du, H.; Du, S.; Li, W. Probabilistic time series forecasting with deep non-linear state space models. *CAAI Trans. Intell. Technol.* **2023**, *8*, 3–13. [CrossRef]
66. Zhao, H.; Ma, L. Several rough set models in quotient space. *CAAI Trans. Intell. Technol.* **2022**, *7*, 69–80. [CrossRef]
67. Chen, J.; Yu, S.; Wei, W.; Ma, Y. Matrix-based method for solving decision domains of neighbourhood multigranulation decision-theoretic rough sets. *CAAI Trans. Intell. Technol.* **2022**, *7*, 313–327. [CrossRef]
68. Hu, X.; Kuang, Q.; Cai, Q.; Xue, Y.; Zhou, W.; Li, Y. A Coherent Pattern Mining Algorithm Based on All Contiguous Column Bicluster. *J. Artif. Intell. Technol.* **2022**, *2*, 80–92. [CrossRef]
69. Zhang, Z.; De Luca, G.; Archambault, B.; Chavez, J.; Rice, B. Traffic Dataset and Dynamic Routing Algorithm in Traffic Simulation. *J. Artif. Intell. Technol.* **2022**, *2*, 111–122. [CrossRef]
70. Hsiao, I.; Chung, C. AI-infused semantic model to enrich and expand programming question generation. *J. Artif. Intell. Technol.* **2022**, *2*, 47–54. [CrossRef]
71. Jia, Z.; Wang, W.; Zhang, J.; Li, H. Contact High-Temperature Strain Automatic Calibration and Precision Compensation Research. *J. Artif. Intell. Technol.* **2022**, *2*, 69–76.

Disclaimer/Publisher's Note: The statements, opinions and data contained in all publications are solely those of the individual author(s) and contributor(s) and not of MDPI and/or the editor(s). MDPI and/or the editor(s) disclaim responsibility for any injury to people or property resulting from any ideas, methods, instructions or products referred to in the content.